The Astrophysical Journal, 919:129 (14pp), 2021 October 1 https://doi.org/10.3847/1538-4357/ac12c8

Lower-luminosity Obscured AGN Host Galaxies Are Not Predominantly in Major-merging Systems at Cosmic Noon

Erini L. Lambrides[1], Marco Chiaberge[1,2], Timothy Heckman[1], Allison Kirkpatrick[3], Eileen T. Meyer[4], Andreea Petric[5], Kirsten Hall[6,14], Arianna Long[7], Duncan J. Watts[8], Roberto Gilli[9], Raymond Simons[5], Kirill Tchernyshyov[10], Vicente Rodriguez-Gomez[11], Fabio Vito[12], Alexander de la Vega[1], Jeffrey R. Davis[1], Dale D Kocevski[13], and Colin Norman[1,5]

[1] Department of Physics and Astronomy, Johns Hopkins University, Bloomberg Center, 3400 North Charles Street, Baltimore, MD 21218, USA
erini.lambrides@jhu.edu
[2] AURA for the European Space Agency (ESA), ESA Office, Space Telescope Science Institute, 3700 San Martin Drive, Baltimore, MD 21218, USA
[3] Department of Physics and Astronomy, University of Kansas, Lawrence, KS 66045, USA
[4] Department of Physics, University of Maryland, Baltimore County, 1000 Hilltop Circle, Baltimore, MD 21250, USA
[5] Space Telescope Science Institute, 3700 San Martin Drive, Baltimore, MD 21218, USA
[6] Atomic and Molecular Physics Division, Harvard-Smithsonian Center for Astrophysics, 60 Garden Street, Cambridge, MA 02138, USA
[7] Department of Physics and Astronomy, University of California, Irvine, CA 92697, USA
[8] Institute of Theoretical Astrophysics, University of Oslo, P.O. Box 1029 Blindern, N-0315 Oslo, Norway
[9] INAF–Osservatorio di Astrofisica e Scienza dello Spazio di Bologna, Via P. Gobetti 93/3, I-40129 Bologna, Italy
[10] Department of Astronomy, University of Washington, Seattle, WA, USA
[11] Instituto de Radioastronomía y Astrofísica, Universidad Nacional Autónoma de México, Apdo. Postal 72-3, 58089 Morelia, Mexico
[12] Scuola Normale Superiore, Piazza dei Cavalieri 7, I-56126, Pisa, Italy
[13] Department of Physics and Astronomy, Colby College, 5800 Mayflower Hill, Waterville, ME 04961, USA
Received 2021 April 7; revised 2021 July 1; accepted 2021 July 7; published 2021 October 4

Abstract

For over 60 yr, the scientific community has studied actively growing central supermassive black holes (active galactic nuclei, AGNs), but fundamental questions on their genesis remain unanswered. Numerical simulations and theoretical arguments show that black hole growth occurs during short-lived periods ($\sim 10^7$–10^8 yr) of powerful accretion. Major mergers are commonly invoked as the most likely dissipative process to trigger the rapid fueling of AGNs. If the AGN–merger paradigm is true, we expect galaxy mergers to coincide with black hole accretion during a heavily obscured AGN phase ($N_{\rm H} > 10^{23}$ cm^{-2}). Starting from one of the largest samples of obscured AGNs at $0.5 < z < 3.1$, we select 40 nonstarbursting lower-luminosity obscured AGNs. We then construct a one-to-one matched redshift and near-IR magnitude-matched nonstarbursting inactive galaxy control sample. Combining deep color Hubble Space Telescope imaging and a novel method of human classification, we test the merger–AGN paradigm prediction that heavily obscured AGNs are strongly associated with galaxies undergoing a major merger. On the total sample of 80 galaxies, we estimate each individual classifier's accuracy at identifying merging galaxies/postmerging systems and isolated galaxies. We calculate the probability of each galaxy being in either a major merger or an isolated system, given the accuracy of the human classifiers and the individual classifications of each galaxy. We do not find statistically significant evidence that obscured AGNs at cosmic noon are predominantly found in systems with evidence of significant merging/postmerging features.

Unified Astronomy Thesaurus concepts: AGN host galaxies (2017); Active galactic nuclei (16); Starburst galaxies (1570); Galaxy mergers (608)

1. Introduction

Supermassive black holes (SMBHs) are in essentially every massive galaxy, and when they are actively accreting matter, known as active galactic nuclei (AGNs), they can potentially inject energy into the gas and expel it and/or prevent it from cooling and collapsing into stars (e.g., Bower et al. 2006; Croton et al. 2006; Heckman & Best 2014). Matter must lose almost all (∼99.9%) of its angular momentum in order to accrete onto the SMBH; thus, studying dissipative processes such as mergers, tidal interactions, stellar bars, and disk instabilities is central to understanding the details of AGN fueling. Despite distinct differences between dissipative processes, neither observational nor theoretical studies converge on a dominant mechanism for funneling matter onto the central SMBH (Jogee 2006). Galaxy mergers with comparable mass ratios (⩾1:4, also defined as major mergers) are one of the most popular mechanisms invoked, yet the observational consensus is mixed. While some empirical and theoretical studies find a connection between mergers and ultraluminous infrared galaxies (Sanders & Mirabel 1996; Veilleux et al. 2009; Lacy et al. 2018), local AGNs (Koss et al. 2010; Ellison et al. 2013, 2019; Gao et al. 2020), high-luminosity AGNs (Urrutia et al. 2008; Treister et al. 2012; Glikman et al. 2015; Donley et al. 2018), and radio-loud AGNs (Chiaberge et al. 2015), others find no connection between mergers and X-ray-detected AGNs (Gabor et al. 2009; Georgakakis et al. 2009), high-luminosity AGNs (Villforth et al. 2014, 2017; Marian et al. 2019), and low-to-intermediate-luminosity AGNs ($L_{\rm bol} < 10^{44}$ erg s^{-1}; Grogin et al. 2005; Schawinski et al. 2011; Rosario et al. 2015).

It is possible that the AGN–merger connection has been systematically missed in some studies due to poor sampling of obscured AGNs. If the AGN–merger paradigm is true, then we can expect a heavily obscured accretion AGN phase to coincide

[14] Schmidt Science Fellow.

with galaxy coalescence (Sanders & Mirabel 1996; Cattaneo et al. 2005; Hopkins et al. 2008). In other words, if a major merger triggers most AGNs, then the AGNs behind large neutral hydrogen column densities ($N_{\rm H} > 10^{23}$ cm^{-2}) should exist in association with the most spectacular phases of mergers.

Obscured sources are inherently difficult to detect in the X-ray, but through the combination of large and deep X-ray surveys with other multiwavelength observations, a large obscured AGN sample can be constructed. The X-ray observations are thought to provide one of the most reliable methods of both selecting AGNs and estimating the amount of AGN obscuration (Brandt & Hasinger 2005; Xue et al. 2011; Liu et al. 2017); however, this is not always true, as Comastri et al. (2011) and Donley et al. (2012) showed that even some of the deepest X-ray surveys miss a substantial fraction (∼40%) of heavily obscured objects.

One of the first studies of its kind, Kocevski et al. (2015) analyzed a sample of obscured AGNs defined using a selection based on X-ray data from the Chandra X-ray Observatory, with the deepest observations at 4 Ms (Xue et al. 2011). Using a single Hubble Space Telescope (HST) near-IR (NIR) band, they found evidence that heavily obscured AGNs are more likely to be in mergers than their less obscured AGN counterparts; point sources included $21.5\%^{+4.2\%}_{-3.3\%}$ heavily obscured AGNs in mergers versus $7.8\%^{+1.9\%}_{-1.3\%}$.

In 2017, the 7MS Chandra Deep-Field South Survey (7MsCDFS), the deepest X-ray survey ever conducted, was released. Within this substantially deeper catalog and the combination of IR, optical, and radio data sets, Lambrides et al. (2020) found that 30% of the X-ray-detected AGNs were misclassified as low-luminosity unobscured AGNs. Lambrides et al. (2020) argued that these objects instead represent the faintest and potentially most obscured AGNs in the 7MsCDFS sample. It is imperative that we morphologically analyze these objects, whose addition may either lend or remove credence to the obscured AGN–merger paradigm.

In this work, we combine the Lambrides et al. (2020) obscured AGN sample with publicly available HST imaging to determine the merger status of the host galaxies of obscured AGNs. The first paper in our series, Lambrides et al. (2021; hereafter L21), introduced a novel statistical method where the accuracy of human classifiers is taken into account in a Bayesian probabilistic framework to determine the merger fraction and individual probabilities of a galaxy being in a merging system. In Section 2, we describe the obscured AGN sample, control sample, HST data, and simulated data used in this work. In Section 3, we describe the survey framework and statistical models used to derive a merger fraction of a population. In Section 4, we present the results of the merger fraction of the obscured AGN population. In Section 5, we discuss how our results compare to other studies and the implications our results have on AGN triggering models. In Section 6, we present the summary and conclusion. We use an $h = 0.7$, $\Omega_m = 0.3$, $\Omega_\Lambda = 0.7$ cosmology throughout this paper. We use the k-sample Anderson–Darling mid-rank statistic to test the null hypothesis that two samples are drawn from the same population and report the test statistic ($D_{\rm ADK}$) significance level at which the null hypothesis for the provided samples can be rejected (Scholz & Stephens 1987).

2. Sample Selection and Data Sets

2.1. Heavily Obscured AGNs

Directly observing X-ray-bright obscured AGNs with the Chandra X-ray Observatory has been possible, especially at energies greater than 2 keV, where X-ray photons are less attenuated by the obscuring material. Generally, X-ray AGNs are commonly selected in the literature as sources with intrinsic X-ray luminosities greater than the maximum luminosity one would expect from host-galaxy emission only (i.e $>10^{42}$ erg s^{-1}) and/or sources with enough X-ray photons in multiple energy bands to robustly model the X-ray spectrum. The latter condition is especially required to estimate the level of attenuation of the X-ray photons. In addition to X-rays, obscured AGNs can also be identified in the mid-infrared (MIR) due to the dust reprocessing of the obscured UV light that emits from the central engine or through polarized scattered light (Houck et al. 2005; Stern et al. 2012; Mateos et al. 2013). The combination of wide and deep X-ray surveys with MIR multiwavelength catalogs has greatly increased the samples of obscured AGNs (e.g., Stern et al. 2005; Donley et al. 2012).

We derive our sample from the Lambrides et al. (2020, hereafter L20) lower-luminosity obscured X-ray AGN catalog. Utilizing the excellent wavelength coverage of the GOODS-S field, L20 analyzed the X-ray luminosities of AGNs from the Chandra 7Ms survey (7MsCDFS) in the context of the radio (VLA 1.4 GHz), optical grism spectroscopy (HST-WFC3), high-resolution optical/NIR imaging and photometry (HST-ACS, HST-WFC3IR), and NIR/MIR/far-infrared (FIR) photometry (Spitzer IRAC, Spitzer IRS PUI, Spitzer MIPS, Herschel PACS). Using the absorption-corrected 2–7 keV X-ray luminosities provided in the Luo et al. (2017) 7Ms catalog, L20 derived an additional absorption correction factor to the X-ray luminosities and thus the $N_{\rm H}$ of each object. This was done by measuring the offset of the Luo et al. (2017) luminosities from the X-ray luminosity required to be in agreement to within 2σ of the Stern (2015) empirical AGN X-ray–to–IR luminosity relationship, where the IR estimate of AGN power is the rest-frame IR luminosity between 3.6 and 5.8 μm. Using the IR excess in combination with X-ray and radio properties, L20 increased the number of identified obscured AGNs in the 7MsCDFS catalog at $0.5 < z < 3$ by 30%, bringing the total number of 7MsCDFS obscured AGNs with $N_{\rm H} > 10^{23}$ cm^{-2} to ∼100.

The 7Ms survey covers an area of ∼290 arcmin^2, and the L20 sample is distributed throughout this field. The Cosmic Assembly Near-IR Deep Extra-galactic Legacy Survey (CANDELS; Guo et al. 2013) and 3D-HST (Skelton et al. 2014) programs and resulting catalogs provide HST coverage for a portion of this field (∼176 arcmin^2). To derive a suitable sample for this work, we first select the portion of the L20 sample that is within HST coverage using the mosaics provided by the 3D-HST[15] (Grogin et al. 2011; Koekemoer et al. 2011; Skelton et al. 2014).

Reliable X-ray–to–HST associations have been found for the CDFS catalog in Luo et al. (2017) using the likelihood ratio technique presented in Luo et al. (2010) with the X-ray full band–derived coordinates. We use the X-ray counterpart F125W-derived coordinates. The counterpart association described in Luo et al. (2010), which takes into account the positional uncertainties of the

[15] https://archive.stsci.edu/prepds/3d-hst/

X-ray and F125W band and expected magnitude distribution of counterparts, has a false-match probability of <4%. From the CANDELS+3D-HST combined catalog, the F125W band has a 5σ limiting AB magnitude of 28.3. We test whether there is a statistical difference in the redshift, X-ray luminosity, and $N_{\rm H}$ distributions of the AGNs with HST coverage compared to the total L20 sample and find that the null hypothesis cannot be rejected where the null hypothesis is that the distributions are identical ($p_{\rm ADK} > 0.25$). The redshifts are provided in the Luo et al. (2017) Chandra 7Ms X-ray catalog; 46 are spectroscopic, and four are photometric. In summary, we find a total of 50 obscured AGNs out of the L20 obscured AGN sample with well-covered ACS F435W, ACS F775W, and WFC3IR F160W imaging data.

2.1.1. X-Ray and MIR Properties

These 50 objects occupy a wide range of X-ray and MIR luminosities. The X-ray and MIR luminosities were derived in L20. The rest-frame MIR luminosity is used as an additional probe of AGN power and defined between 3.2 and 5.7 μm. The AGN torus emission dominates over MIR star formation (SF) processes in this wavelength range, which is especially pertinent for lower-luminosity, moderate-redshift AGNs where other photometric MIR diagnostics may fail to capture these objects (Laurent et al. 2000; Nenkova et al. 2008; Kirkpatrick et al. 2012; Lambrides et al. 2019). In L20, the rest-frame AGN MIR luminosity, referred to as $L_{\rm torus*}$, is calculating the photometric luminosity of a single data point using the passband that most closely corresponds to the rest-frame wavelength range of interest. For the range of redshift spanned by our sample, the passbands used are the IRAC 8 IRS PUI 16 and MIPS 24 μm, and, for further details on the MIR cross-matching and rest-frame luminosity calculation, we refer the reader to the aforementioned paper.

In Figure 1, we show the non-absorption-corrected X-ray luminosities compared to the AGN luminosity in the MIR ($L_{\rm torus*}$). The red shaded region corresponds to the unobscured AGN region of the parameter space. This is defined by the range in intrinsic X-ray, rest AGN MIR luminosity relationships between two different X-ray–to–MIR relationships: Gandhi et al. (2009) and Fiore et al. (2009). The Gandhi et al. (2009) relationship was derived from a local sample of type 1 AGNs ($0.03 < z$, 8×10^{41} erg s$^{-1} < L_{\rm X} < 4 \times 10^{43}$ erg s^{-1}), and decomposition of the nuclear 6 μm luminosity was performed to minimize host-galaxy contamination. The Fiore et al. (2009) relationship was derived from a sample that spanned a larger redshift and X-ray luminosity range as compared to Gandhi et al. (2009; $0.7 < z < 2.2$, 3×10^{43} erg s$^{-1} < L_{\rm X} < 10^{45}$ erg s^{-1}) and did not include host-galaxy decomposition of the 6 μm luminosity. Due to the inherent uncertainties of these relationships, instead of choosing a single empirical relationship, L20 chose a conservative approach and instead used both of these relationships to determine a region of the parameter space that corresponded to less obscured AGNs. The heavily obscured region indicates the same empirical relationships, but the X-ray luminosity is scaled down to represent a column density of $N_{\rm H} > 10^{24}$ cm^{-2} (Lansbury et al. 2015).

The blue points in Figure 1 comprise the heavily obscured AGN subsample from L20 with HST coverage and are not significantly starbursting, as described in the previous section. In the next section, we discuss the motivation and the removal of AGN host galaxies with starbursts (SBs).

2.1.2. Removing SBs

A multitude of theoretical and observational evidence has accumulated that potentially connects galaxy mergers and interactions to extreme bursts of SF or SB (Hibbard & van Gorkom 1996; Sanders & Mirabel 1996; Hopkins et al. 2006; Davies et al. 2015; Cortijo-Ferrero et al. 2017; Moreno et al. 2019; Pearson et al. 2019). The purpose of this work is to test the prediction that obscured AGNs are more likely to be found in galaxies that are undergoing a significant merger. If there is a direct causal connection between mergers and SF and a star formation rate (SFR) matched control sample is not used, an apparent secondary correlation between AGNs and mergers can be induced. Thus, assessing the SF properties of the obscured AGN sample and the matched control sample is paramount. It is difficult to calculate robust SFRs of AGN host galaxies from photometry alone, and a careful analysis of the SF properties of the obscured AGN hosts is outside the scope of this paper due to the type of data in hand. Therefore, we identify sources that are likely undergoing the most extreme episodes of SF for a given stellar mass and redshift and isolate them from the main sample. Due to the small number of obscured AGNs with SBs in their hosts, our main analysis will focus on the non-SB obscured AGN sample. The scope of this work is to test the hypothesis that the majority of obscured AGNs are predominantly triggered by significant galaxy mergers. In Section 5, we explore the merger properties of the SB obscured AGN sample and the implications of an SB–AGN merger connection versus a non-SB–AGN merger connection.

From this sample of 50 obscured AGNs with HST coverage, we then select objects that are likely to be either on the SF main sequence or quiescent. Utilizing the extensive wavelength coverage of the GOODS-S field, we calculate the position of the obscured AGNs relative to the SF main sequence for each galaxy's redshift and stellar mass. The stellar masses of the sample are given in the 3D-HST survey catalog (Skelton et al. 2014). As described in Skelton et al. (2014), these authors used the FAST code (Kriek et al. 2009) to estimate the stellar properties of the entirety of the GOODS-S field. Due to the obscured nature of the AGNs, the derived stellar masses are more robust than the other stellar properties estimated in the catalog.

As is stressed in Skelton et al. (2014), the SFRs are uncertain when they are derived solely from optical-NIR photometry. Since our obscured sample is heavily obscured ($N_{\rm H} > 5 \times 10^{23}$ cm^{-2}), the stellar masses are well constrained, as they predominantly depend on the rest-frame optical fluxes of the galaxies where there is negligible contamination from the central engine. The redshift range of our sources and the multiple HST band coverage allow for the rest-frame optical fluxes of our galaxies to be well measured. To estimate the SFR in our galaxies, we use the detections (or lack of) in the FIR. The FIR is a more unbiased indicator of SF than the MIR in AGN host galaxies because the contribution from nuclear hot dust heated by the AGN contributes <20% at >100 μm even for the most powerful AGNs (Kirkpatrick et al. 2015; Dai et al. 2018; Brown et al. 2019). In this work, we estimate the SFR as traced by the 100 and 160 μm Herschel PACS bands, utilizing the redshift information of the source and the SFR calibration provided in Calzetti et al. (2010). The coverage and detection

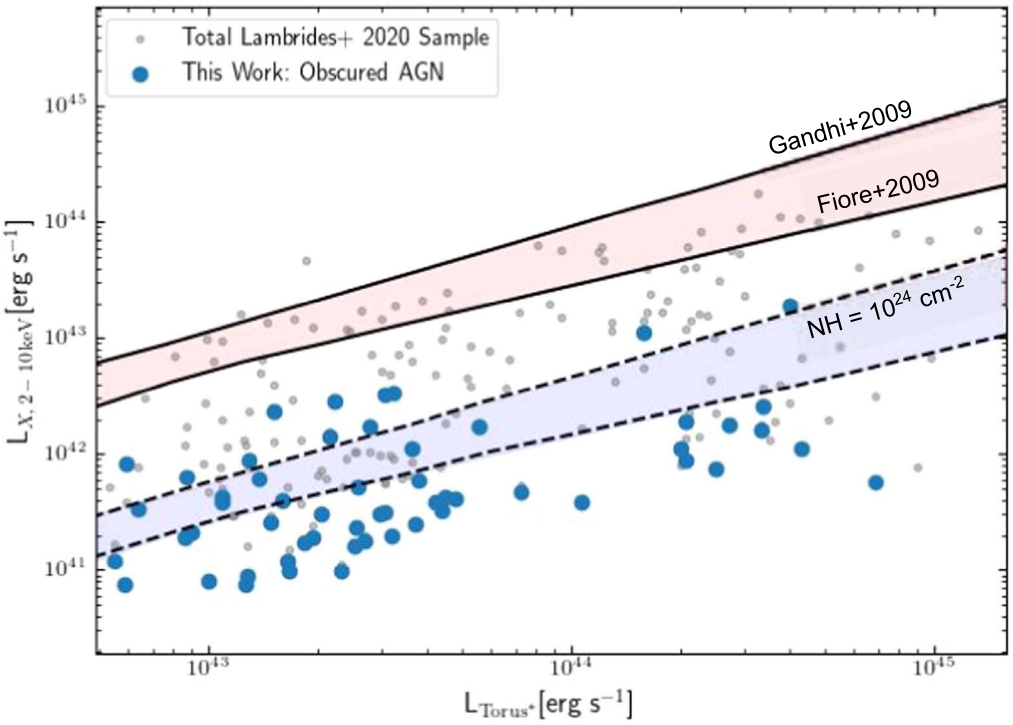

Figure 1. Non-absorption-corrected X-ray luminosity vs. rest-frame AGN MIR luminosity. Obscured AGN candidates straddle or lie below the blue shaded region. As adapted by Lansbury et al. (2015), the unobscured region parameter space (red) indicates the range in intrinsic X-ray, 6 μm AGN luminosity relationships between Gandhi et al. (2009) and Fiore et al. (2009). The heavily obscured region (blue) indicates the same relationships but where the X-ray luminosity is absorbed by a column density of $N_{\rm H} > 10^{24}$ cm^{-2} (Lansbury et al. 2015)

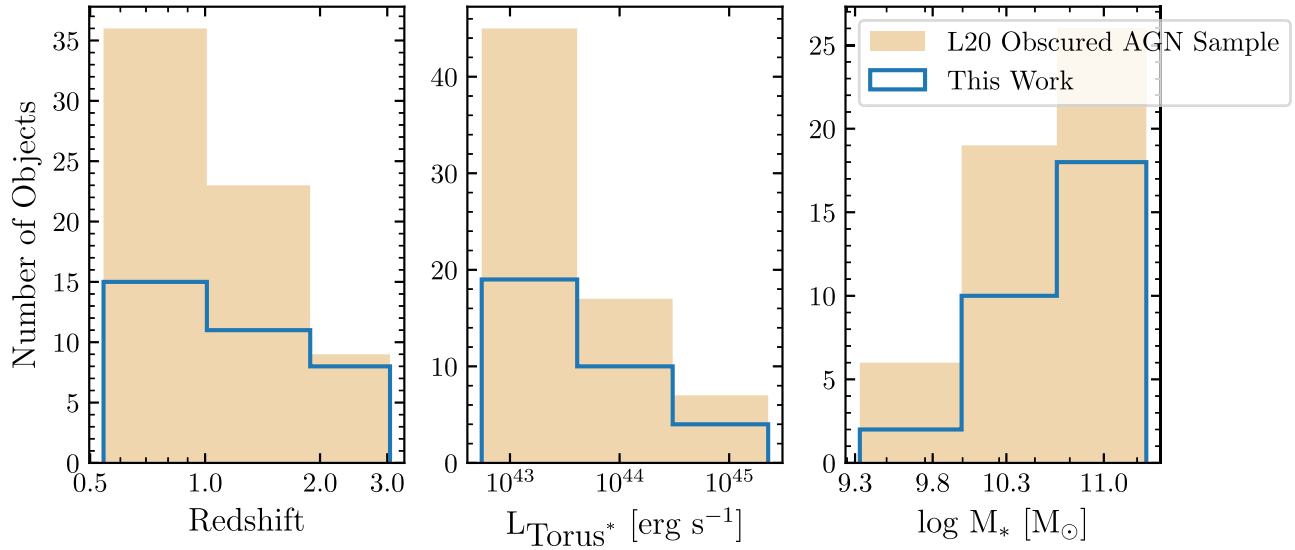

Figure 2. Parent sample and this work. Shown is a comparison of properties of the L20 obscured AGN sample to the nonstarbursting, HST-covered subsample used in this work.

of the AGN sample at such wavelengths are discussed in L20. For objects with nondetections, we estimate the SFR using $\mathrm{SFR}_{160\ \mu\mathrm{m}}\ M_\odot\ \mathrm{yr}^{-1} = L_{160\ \mu\mathrm{m}}/7 \times 10^{42}$ for $L_{160\ \mu\mathrm{m}} > 2 \times 10^{42}$ erg s^{-1} $\sim 5.2 \times 10^8\ L_\odot$. For the 31 nondetections, we estimate the SFR upper limit by calculating the $L_{160\ \mu\mathrm{m}}$ upper limit using the 3σ average depth limit of 2.7 mJy as presented in Elbaz et al. (2011).

We then use the SFR relation for main-sequence galaxies presented in Schreiber et al. (2015) to calculate the SFR of the main-sequence galaxies at each object's mass and redshift. The SBs are defined as 0.6 dex above the main-sequence population for a given stellar mass, SFR, and redshift (Rodighiero et al. 2011). Of the 50 obscured AGNs, we remove from the sample the sources that are 0.6 dex or more above their main-sequence counterpart. This leaves the final non-SB obscured AGN sample with 40 objects.

In Figure 2, we show a comparison of the redshift, L_{torus^*}, and stellar mass distributions of the L20 parent sample compared with the limited sample used in this work. We calculate the k-sample Anderson–Darling mid-rank statistic between the redshift, L_{torus^*}, and stellar mass distributions of the L20 sample of heavily obscured AGNs to the subsample

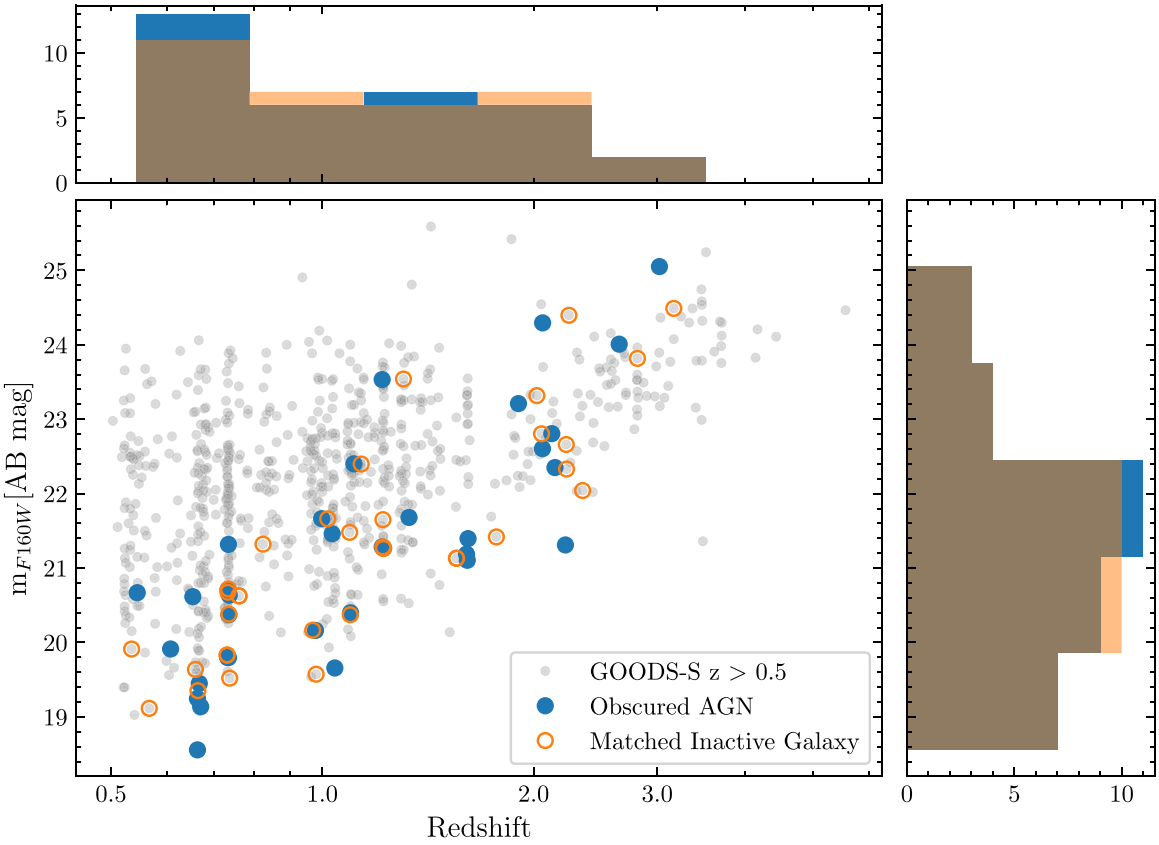

Figure 3. The F160W AB magnitude versus redshift. The gray points are the entirety of the 7Ms sample with HST coverage for $z > 0.5$ in GOODS-S. The blue points are the redshifts and F160W magnitudes of the non-SB obscured AGN sample. The orange points are for the counterpart inactive galaxy control sample.

used in this work and find that the null hypothesis cannot be rejected; thus, the sample used in this paper is representative of the obscured AGNs found in the larger 7Ms survey.

2.2. Control Sample

Since the goal of this work is to measure any significant excess of mergers in the obscured AGN sample as compared to nonactive galaxies, a control sample must be carefully selected to closely match the properties of the AGN hosts. We one-to-one match the non-SB obscured AGNs to non-AGN galaxies (within $\Delta_{m_{\rm F160W}} \pm 0.5$, $\Delta_z \pm 0.5$) using the 3D-HST photometry catalog (Skelton et al. 2014) and spectroscopically secure redshifts from Momcheva et al. (2016). If multiple galaxies satisfy the $\Delta_{m_{\rm F160W}}$, Δ_z criteria, we select the galaxy with the smallest difference. The mean differences of $\Delta_{m_{\rm F160W}}$ and Δ_z between the non-SB obscured AGN sample and the counterpart sample are -0.04 and -0.03, respectively. We choose only one counterpart galaxy per non-SB AGN to ensure that the total sample is of reasonable size for visual classification. We use this non-AGN galaxy sample, herein called the control sample, to assess the presence of an obscured AGN–merger connection.

Matching the control galaxy sample to the SF properties of the AGN host galaxies is a necessity. We remove SB galaxies from the catalog as described in the previous section. In Figure 3, we show the redshift and F160W magnitude distribution of the non-SB obscured AGN sample (blue points), control sample (orange points), and the entire $z > 0.5$ GOODS-S field with SBs and galaxies with photometric redshifts included (gray points). We find that the distributions in redshift and magnitude are statistically indistinguishable between the non-SB obscured AGNs and the control sample; the null hypothesis that the two samples are drawn from the same distribution in both z and Ks magnitudes cannot be rejected ($p_{\rm ADK} > 0.25$). In Figure 3, we include the total GOODS-S $z > 0.5$ sample to visually compare the region of the parameter space the non-SB obscured AGN and counterpart sample occupies to the inactive galaxies not matched to the non-SB obscured AGN sample.

To summarize, we cross-match a nonstarbursting, HST-covered subsample of the L20 obscured AGN catalog to the CANDELS+3D-HST combined HST GOODS-S catalog (Skelton et al. 2014; Momcheva et al. 2016). The HST-covered L20 subsample consists of 40 non-SB obscured AGNs with 34 spectroscopic redshifts and six photometric redshifts. The control sample consists of 40 nonactive redshift, $\rm mag_{F160W}$ matched counterpart galaxies, all with spectroscopic redshifts. The distributions of the non-SB obscured AGN sample and control sample distributed in redshift and F160W magnitude space are statistically identical with $0.5 < z < 3.1$ and $18.2 < \rm mag_{F160W}[AB] < 25.1$.

2.3. HST Data Sets

The number density of obscured AGNs is inferred to peak in the range $1 < z < 2$ (e.g., Gilli et al. 2007; Aird et al. 2015). Beyond optical $z \sim 1$ imaging, surveys begin to probe the rest-frame UV morphologies of galaxies. This is useful for probing the most active regions of unobscured SF but may miss the gaseous and stellar features associated with merging systems (i.e shells, disk asymmetry). An additional complication with morphologically analyzing $z > 1$ galaxies is the increasing

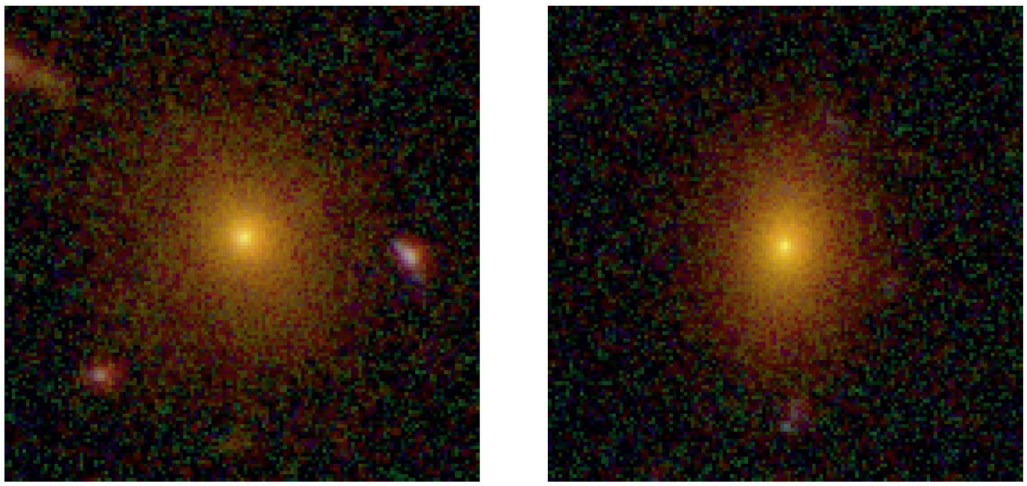

(a) Obscured AGN: ID 642 from Luo et al. (2017)

(b) Counterpart Non-AGN Galaxy: ID 18169 via Skelton et al. (2014)

Figure 4. Example of sample imaging. Shown are the obscured AGN RGB image at $z = 0.7$ (a) with its z and the F160W matched non-AGN galaxy counterpart (b).

incidence of foreground and background galaxies near the region of the object of interest. Color images are helpful in determining whether a close pair is a random superposition of galaxies or two galaxies at the same redshift. Thus, we need multiple optical/UV imaging bands at similar depths in order to assess the merger status of a $z > 1$ galaxy.

In this study, we use the 3D-HST reduced and combined GOODS-S mosaics (Skelton et al. 2014). We make a $6'' \times 6''$ cutout centered on the X-ray coordinates for the obscured AGN sample and the 3D-HST coordinates for the control sample. Each of the postage stamps was individually inspected to ensure no prominent image artifacts were in the cutouts. In Figure 4, we show an example of imaging from the obscured and matched control sample. All of the postage stamps of the obscured and control sample in this study are made publicly available.[16]

2.4. Mock Galaxy Sample

An important aspect of merger classification studies is the major uncertainty associated with the accuracy of human classifiers. By accuracy, we mean the ability of each person to correctly identify mergers and disentangle them from random superpositions, asymmetries in galaxy structure not due to tidal interactions, and relaxed morphologies. Even if the classifiers are experts and proper statistical analysis is performed to remove outliers (e.g., using trimmed means as in Chiaberge et al. 2015), a bias can still be present. It was found by L21 that when using one of the most standard statistical implementations to calculate the merger fraction in the literature, the effective bias due to humans is dependent on the intrinsic merger fraction of a given sample. The implications of this result cast doubt on the sole usage of a control sample as a justifiable means to encapsulate human bias. Authors L21 proposed a method of quantifying and accounting for the merger biases of individual human classifiers and incorporated these biases into a full probabilistic model to determine the merger fraction of a population and the probability of each individual galaxy being in a merger. In Section 3.2, we summarize the formalism and results of L21 on the definition and effect of the bias introduced by human classifiers in addition to the statistical framework used to infer the merger fraction of a sample.

In L21, we introduced a new method to calibrate the accuracy of human classifiers. An estimate of the classifiers' accuracy was used as a prior in determining the merger fraction of a galaxy sample. The accuracy priors were determined using simulated images from the VELA cosmological simulations (Ceverino et al. 2014; Snyder et al. 2015; Simons et al. 2019). As shown in L21, 50 mock images in three different bands (two in the optical and one in the NIR) were produced with the appropriate amount of Poisson noise to simulate the real data sets used in this research. The mock galaxy sample has the same redshift distribution as the non-SB obscured AGN sample used in this work. With their origin hidden, these simulated observations were also classified by each of the coauthors in this work, and for more details on the construction of the mock images, we refer the reader to L21.

3. Determining a Data-driven Merger Fraction

At $z > 1$, it becomes more difficult to accurately assess the merger state of a galaxy, as faint merger signatures may be undetectable (Lotz et al. 2004). Despite the great potential of automated methods such as deep learning for merger identification, there currently is no tool that is robust enough to handle the diverse presentations of merging galaxies in the earlier universe (Pearson et al. 2019). Visual human classification is the most commonly employed method used to identify moderate samples of merging galaxies at $z > 1.0$, but rarely if ever do the authors of these studies attempt to control for human bias in morphological studies aside from the use of a control sample.

In L21, we used simulated and observed data sets to create and validate a data-driven merger fraction probability model, where the merger fraction is defined as the fraction of galaxies within a given sample undergoing a significant merger. For the observed data sets, we used real human classifications on a sample of mock images with known truth values derived from cosmological simulations. We found that the bias introduced

[16] erinilambrides.com/morphology_of_obscured_agn

from human classification is dependent on the intrinsic merger fraction of the population, and not accounting for this bias can drive the resulting merger classification rates to be significantly different from the intrinsic truth. The statistical framework posed in L21 accounts for the merger classification biases of individual human classifiers, and these biases are then incorporated into a full probabilistic model to determine the merger fraction of a population and the probability of an individual galaxy being in a merger. In this section, we describe how the human classification of the non-SB obscured AGNs and inactive galaxy counterpart sample were collected and analyzed using the L21 framework.[17]

3.1. Object Classification Method

We developed a website where classifiers could assess the morphologies of the non-SB obscured AGN, control, and mock galaxy samples without knowing which sample an object came from. The Morphology of Obscured AGN (or MOOAGN) classifying framework comprises the entirety of the sample: 40 obscured AGNs, 40 matched inactive galaxies, and 50 mock galaxies. We also provided a demo survey of five objects (not used in the MOOAGN sample) to give the classifiers a reference framework of the classification options and data quality. At the end of the demo survey, we give some example justifications of why one would classify an object as such (see the Appendix for the demo survey and example classifications). Ultimately, for our analysis, we use only two morphological classes: merging and not merging. Due to the difficulty in constraining the merger stage and mass ratio given the data in hand, further morphological subdivisions would yield potentially less accurate results. Nonetheless, when the human classifiers are presented with the images, they are given multiple morphological divisions to choose from. This is to not only aid in the human classification process but also to take the most conservative approach of testing for a merger excess in non-SB obscured AGN host galaxies. We assume that any system with obvious merging features observed at these redshifts must be a significantly merging system. If we are incorrect with this assumption, then the merger fraction would be lower for major-merging systems. After the sample was classified, the divisions were folded back into the two morphological classes of merging or not merging. The five classification options given to the human classifiers are as follows.

1. Merging: major (approximately similar size). Ongoing interaction. This is prior to coalescence, i.e., two distinct interacting galaxies of similar size. Features for this classification can include tidal tails with distinct galaxy pairs, enhanced SF, and morphological distortion along the closest axis of approach between two pairs.
2. Merging: minor (approximately <1:4 size ratio). Similar to the major merger classification with the exception of size. If a galaxy pair has evidence of interaction, and one of the bodies is roughly less than one-fourth the size of the larger galaxy, it is classified as a minor interaction.
3. Disturbance: major. Intended to capture galaxies that have coalesced within 100 Myr. Features can include highly irregular gas/stellar morphologies and tidal tails with only one distinct central bulge.
4. Disturbance: minor. Intended to capture galaxies that are slightly irregular yet indistinguishable from internal processes that could cause the irregularity, i.e., star-forming clumps and disk instabilities.
5. No evidence of merger/interaction.

Examples of galaxies fitting the above criteria are shown in the Appendix. We then collate the classifications of our 14 human classifiers of all 130 objects on the MOOAGN sample.

3.2. Calculating the Merger Fraction Likelihood

As previously mentioned, even among experts, it is difficult to accurately characterize whether a galaxy is undergoing a merger or is isolated. Because of this, it is inevitable that any given classifier will obtain a merger fraction that is different from another classifier's assessment. For example, one may be more inclined to classify objects as mergers even if the objects display minor disturbances unrelated to galaxy encounters. It was assumed by L21 that the bias of human classifiers can be quantified in terms of their accuracy in correctly classifying an intrinsically merging galaxy as a merger (and an intrinsically isolated system as isolated). Previous works have assumed that the effect of this bias on independent galaxy samples is similar (i.e., if the same set of humans are classifying a science and a control sample, the assumption is that the bias due to human classification is equally present in both samples). Thus, due to this assumption, and to account for other unquantified biases such as those potentially introduced during the method of selecting the science sample in the first place, most merger studies do not report absolute merger fractions of a specific population but rather compare the merger fraction of the science sample to a well-justified control sample. The control sample in this context is any sample of sources that lacks the key feature that defines the science population in question but shares any relevant properties that might be correlated with the morphology or presentation of the morphology of an object (i.e., redshift, stellar mass, SFR, etc). Though, as shown in L21, if the underlying merger fraction of the two populations (i.e., science and control) are significantly different, this human bias will not be evenly applied. Therefore, the bias introduced by using human classifiers will still be present in any statistical comparison between the merger fractions of the science and control samples.

Summarizing the L21 characterization of this bias, if one is shown a merging (or isolated) galaxy, one will classify the galaxy correctly with probability r_M (or r_I). Therefore, if somebody is shown N_M intrinsic mergers and N_I intrinsic isolated galaxies, on average, that person will measure $\hat{N}_M = r_M N_M + (1 - r_I)N_I$ mergers. The inclusion of the $(1 - r_I)N_I$ term represents the number of galaxies that were incorrectly classified as isolated and are truly mergers.

Using the formalism of r_M (or r_I) to characterize the bias of human classifiers, L21 showed that the use of relative significance between comparing the merger fractions of the science and control samples does not remove this issue. By rewriting the measured $\hat{N}_M$ and $\hat{N}_{M,c}$ in terms of the measured merger fraction for each sample and the intrinsic value of N_M and $N_{M,c}$ in terms of the intrinsic merger fraction f_M of each sample and taking the difference

$$\langle \hat{f}_M \rangle = r_M f_M + (1 - r_I)(1 - f_M), \quad (1)$$

$$\langle \hat{f}_{M,c} \rangle = r_M f_{M,c} + (1 - r_I)(1 - f_{M,c}), \quad (2)$$

[17] The full source code of the likelihood maximization can be found here: https://github.com/elambrid/merger_or_not.

$$\langle \Delta \hat{f}_M \rangle = \langle \hat{f}_M \rangle - \langle \hat{f}_{M,c} \rangle, \tag{3}$$

$$\begin{aligned} \langle \Delta \hat{f}_M \rangle &= r_M \Delta f_M - (1 - r_I) \Delta f_M \\ &= \Delta f_M [r_M + r_I - 1], \end{aligned} \tag{4}$$

they found that the difference between the measured merger fractions of the two samples is still dependent on the intrinsic merger fraction of each sample.

Using the merger fraction likelihood algorithm presented in L21, we are able to infer the underlying merger fraction by using a novel technique to quantify the bias of each individual classifier. We then optimally combine the individual classifier uncertainties with the individual classifications of each galaxy in the sample. In the merger fraction statistical model presented in L21, classifier accuracy is a nuisance parameter that can be marginalized over. Further details on the construction of the algorithm can be found in the aforementioned work. We briefly summarize the algorithm here.

A respondent i is shown a true merger, and that respondent classifies it as a merger with probability r_M or an isolated galaxy with probability $1 - r_M$. Conversely, if the respondent is shown a true isolated galaxy, the respondent will say that it is a merger with probability $1 - r_I$ or isolated with probability r_I. Thus, respondent i classifies the jth galaxy G_j with classification m as

$$p(m_i|G_j) = \begin{cases} r_M & m_i = G_j = \text{merger} \\ 1 - r_M & m_i \neq G_j = \text{merger} \\ r_I & m_i = G_j = \text{isolated} \\ 1 - r_I & m_i \neq G_j = \text{isolated} \end{cases}. \tag{5}$$

The likelihood of the classifications of a single galaxy by multiple classifiers given a merger fraction and classifier accuracies can be written as

$$\begin{aligned} p(\{m_i\}|\{r_i\}, f_M) = f_M \prod_i p(m_i|G_j = \mathrm{M}) \\ + (1 - f_M) \prod_i p(m_i|G_j = \mathrm{I}), \end{aligned} \tag{6}$$

where f_M is the merger fraction of a given population and index i corresponds to an individual classifier. In this expression, the true nature of the galaxy in question is marginalized out. Expanding to multiple galaxies, we get the likelihood for the classifications of a collection of galaxies:

$$p(\{m_{ij}\}|\{r_i\}, f_M) = \prod_j p(\{m_{ij}\}|\{r_i\}, f_M). \tag{7}$$

Multiplying this likelihood by a prior on the merger fraction and, if the classifier accuracies are not held fixed, by a prior on accuracies gives the unnormalized posterior probability distribution function for this model. If we wish to recover the probability that a particular galaxy is a merger, we can use the expression

$$p(G = M|\{m_i\}, \{r_i\}, f_M) = \frac{f_M \prod_i p(m_i|G = M)}{p(\{m_i\}|\{r_i\}, f_M)}. \tag{8}$$

The probability that this galaxy is isolated is the complement of this expression. This expression is evaluated with an informative prior on the accuracies r_M and r_I. The prior is determined from the classifications of the mock galaxies, which have known merger states. We refer the reader to L21 for further details on the derived r_M and r_I classifications. The same set of human classifiers was used in both L21 and this work, and the mean priors of r_M and r_I are 0.74 and 0.63, respectively.

The strength of this method is its internal consistency; given a set of observed mergers, the likelihood is maximized when a value of f_M shown to all classifiers is most plausible, given a prior on classifier accuracies and the individual classifications of each galaxy. For example, in studies that determine the merger fraction of a population from a set of galaxies classified by a set of human classifiers, the merger fractions from each classifier are collated, and the error treatment uses the standard binomial statistics. In this scenario, it is possible for classifiers to identify a similar number of mergers but be in disagreement with each other on the classification of individual objects. This lack of interclassifier agreement would not be encapsulated in the standard error treatment. In the method utilized in this work, the determination of the most plausible f_M requires determining the most plausible classification of each individual galaxy.

The likelihood function of a given galaxy having a specific morphological classification requires a robust statistical description of a human classifier's accuracy in assessing both merging and isolated systems. In the previous step, where we maximize the likelihood of a population's merger fraction, our algorithm also maximizes the likelihood of an individual galaxy's classification. This allows for deeper data exploration on galaxy samples that are normally too small to do anything but population averages.

4. The Non-SB Obscured AGN Merger Fraction

We first present the merger fractions of the non-SB obscured AGN and the sample of control objects without taking into account the accuracies of the human classifiers. We take the mean number of galaxies classified as either a major merger, minor merger, or majorly disturbed system from each of the 14 classifiers. We also report the binomial confidence interval at the 68% level, or 1σ, using the Jeffreys interval, a Bayesian application to the binomial distribution (Brown et al. 2001). The merger fraction and corresponding 1σ error of the non-SB obscured AGN sample is $0.59^{+0.06}_{-0.10}$. For the control sample, the merger fraction and 1σ error is $0.53^{+0.06}_{-0.11}$. The merger excess of non-SB obscured AGNs over a matched inactive control sample is $1.1^{+0.3}_{-0.2}$. Thus, using the standard binomial method, the control and obscured samples are not statistically separable. Yet, as shown in L21, the only instance in which the relative comparison of two merger fractions using the standard binomial method is not biased due to human classification is when the two samples being compared have the same intrinsic merger fraction. Since we do not know a priori the intrinsic merger fractions of the non-SB obscured AGN and control sample, we must use our newly derived method to estimate the merger fraction.

Thus, we use the merger fraction likelihood framework presented in L21 and summarized in Section 3.2 to simultaneously calculate the probability of the merger fraction of each subsample, the probability distribution of each classifier's accuracy in measuring merging and isolating systems, and the probability of each individual galaxy being in a merger. In Figure 5, we report the merger fraction probability distribution of the non-SB obscured AGN and control sample being in an merging system. The y-axis probabilities are normalized such that the area under the distribution curve is equal to 1. We find that the non-SB obscured AGN sample has a merger fraction

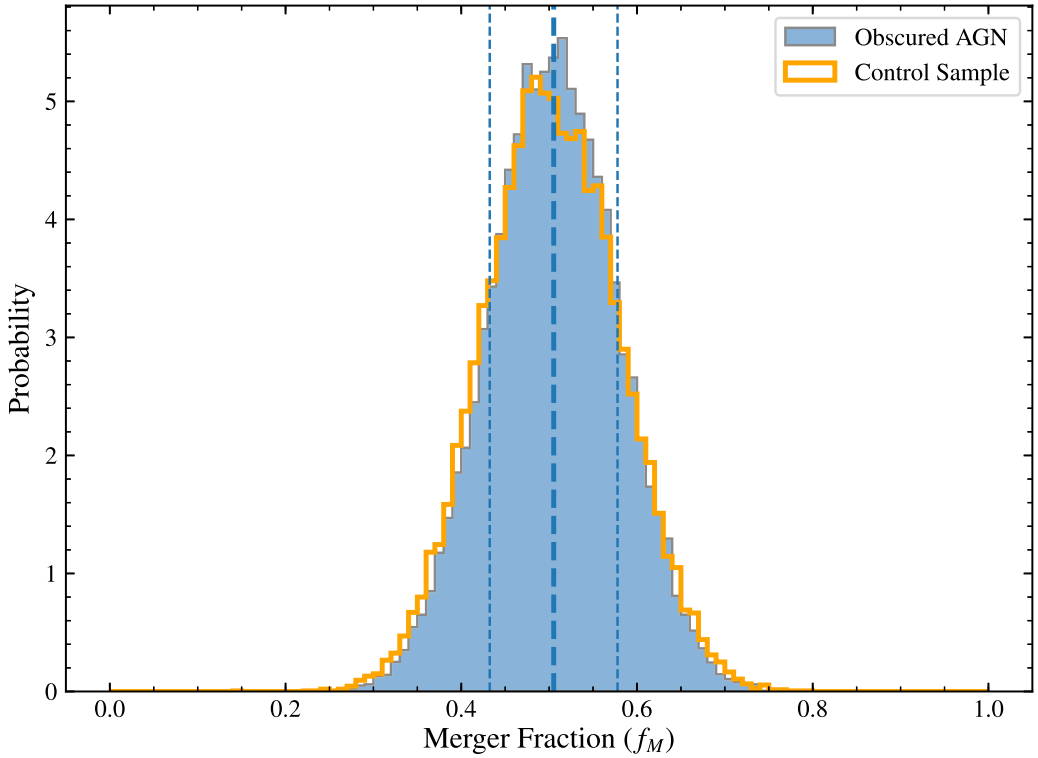

Figure 5. Merger probabilities of non-SB obscured AGN and inactive galaxy control sample. We use the method presented in Section 3.2 to calculate the probabilities of each individual galaxy in the non-SB obscured AGN and control samples being in a merging system. The thick dashed blue line is centered on the mean of the AGN distribution, with the two thin blue dashed lines representing the 85th percentile on either side of the mean. The blue line is centered at the mean of the obscured AGN distribution, with the blue dashed lines representing the 85th percentile. There is no significant difference in the merger fractions.

probability of $54\% \pm 8\%$, and the inactive galaxy control sample is found to have a $53\% \pm 9\%$ mean probability of being in a merger.

The main result of our work is as follows. The obscured AGN merger fraction is statistically indistinguishable from the control sample merger fraction ($<1\sigma$).

In the following subsections, we explore whether an intrinsic difference exists between the merger state of obscured and inactive galaxies as a function of various galaxy properties. We test the extent of the dependence on merger probability on different galaxy and AGN properties by simply splitting the subsample along the 50th percentile (or on either side of the median) of the property being explored. We do this to have enough objects in each bin to keep the error on the subsample size small enough for meaningful comparison and to minimize assumptions on bin width.

4.1. Redshift Dependence

We first compare whether there is a difference in the merger fractions as a function of redshift. We split the non-SB obscured AGN sample along the median, $0.5 < z < 1.1$ (20 objects) and $1.1 < z < 3.5$ (20 objects), and split the control sample along those same bin definitions (the redshift median of the control sample is also 1.1, with 20 objects in each bin). In Figure 6, we show the merger probabilities of the non-SB obscured AGN and control sample for each redshift bin. For the lower redshift bin, we find $f_M = 0.42 \pm 0.11$ and 0.44 ± 0.12 for the non-SB obscured AGN sample and matched control sample, respectively. For the higher redshift bin, we find $f_M = 0.51 \pm 0.11$ and 0.49 ± 0.12 for the non-SB obscured AGN sample and matched control sample, respectively. We do not find any statistical difference between the non-SB obscured AGN sample and the control sample for either the lower or higher redshift bin ($<1\sigma$ difference).

4.2. Galaxy Stellar Mass Dependence

We next explore whether there is any difference in the merger probabilities between non-SB obscured AGN and the control sample that is dependent on stellar mass. In Figure 7, we again split the non-SB obscured AGN sample on the median log stellar mass: $9.32 < \log\,(M_*\ [M_\odot]) < 10.7$ (20 objects) and $10.7 < \log\,(M_*\ [M_\odot]) < 11.32$ (20 objects). Using the same bin widths, we split the control sample (20 objects). For the lower-mass bin, we find $f_M = 0.39 \pm 0.19$ and 0.45 ± 0.22 for the non-SB obscured AGN sample and matched control sample, respectively. For the higher-mass bin, we find $f_M = 0.55 \pm 0.15$ and 0.49 ± 0.28 for the non-SB obscured AGN sample and matched control sample, respectively. We find that again, the difference between the non-SB obscured AGN sample and the control sample is not statistically significant ($<2\sigma$ difference).

4.3. Dependence on Obscuration and AGN Power

We then test whether there is any difference in merger probabilities for different levels of AGN obscuration and/or power. In Figure 8, we split the non-SB obscured AGN sample along the median of obscuration to produce two bins of less obscured AGNs (22 objects) versus more obscured AGNs (25 objects). For the lower- and higher-$N_{\rm H}$ bins, we find $f_M = 0.48 \pm 0.11$ and 0.47 ± 0.11, respectively. We do not find a

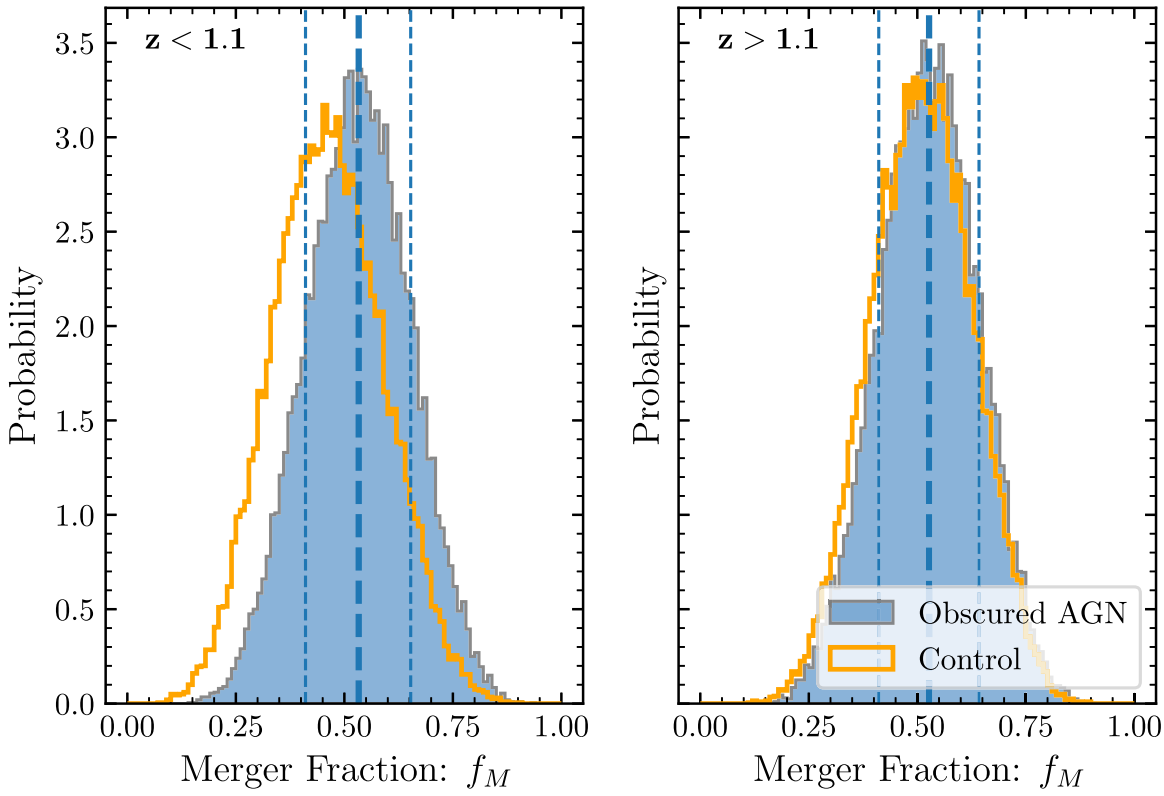

Figure 6. Merger probabilities of the non-SB obscured AGN and inactive galaxy control sample in two redshift bins. The blue filled histogram is the merger probability distribution of the non-SB obscured AGN sample, and the open orange histogram is the matched inactive galaxy sample. The left panel represents objects in the lower 50% of the redshift distribution ($0.5 < z < 1.1$; 20 objects), and the right panel shows the merger probability distributions for the objects in the upper 50% of the sample redshift distribution ($1.1 < z < 3.5$).

significant difference among the extremely obscured objects versus the moderately obscured objects, as the merger fractions are consistent with each other to better than 1σ. As an additional test, we compare the lower- and higher-$N_{\rm H}$ bins against each of their respective matched control samples. For the lower-$N_{\rm H}$ bin, we find $f_M = 0.48 \pm 0.11$ and 0.46 ± 0.10 for the non-SB obscured AGN sample and matched control sample, respectively. For the higher-$N_{\rm H}$ bin, we find $f_M = 0.47 \pm 0.13$ and 0.43 ± 0.25 for the non-SB obscured AGN sample and matched control sample, respectively.

We also test whether there is a difference among the more powerful AGNs in our sample versus less powerful AGNs. As in L20, we use $L_{\rm torus^*}$, a rest-frame 5 μm luminosity indicator, to probe AGN power. In Figure 9, we show the merger probabilities of the non-SB obscured AGN split along the median value of $L_{5\ \mu{\rm m}}$: $5.5 \times 10^{42} < L_{5\ \mu{\rm m}}$ (erg s^{-1}) $< 2.7 \times 10^{43}$ (32 objects) and $2.7 \times 10^{43} < L_{5\ \mu{\rm m}}$ (erg s^{-1}) $< 2.3 \times 10^{45}$ (34 objects). For the lower- and higher-$L_{5\ \mu{\rm m}}$ bins, we find $f_M = 0.37 \pm 0.25$ and 0.47 ± 0.31, respectively. For the 5 μm rest-frame luminosity values we probe in our sample, we do not find a significant difference between the two bins of non-SB obscured AGNs, as the merger fractions are consistent with each other to better than 2σ. We then compare the lower- and higher-$L_{5\ \mu{\rm m}}$ bins against each of their respective matched control samples. For the lower-$L_{5\ \mu{\rm m}}$ bin, we find $f_M = 0.49 \pm 0.12$ and 0.47 ± 0.10 for the non-SB obscured AGN sample and matched control sample, respectively. For the higher-$L_{5\ \mu{\rm m}}$ bin, we find $f_M = 0.51 \pm 0.12$ and 0.48 ± 0.16 for the non-SB obscured AGN sample and matched control sample, respectively.

5. Discussion

In terms of merger fraction, we do not find any significant difference between our non-SB obscured AGN sample and a redshift, F160W, nonstarbursting, non-AGN galaxy sample. This is in tension with both theoretical and observational works that place heavily obscured AGNs within a major merger–driven evolutionary paradigm. It has been speculated that the AGN–merger connection may have been systematically missed due to poor sampling of obscured AGNs (Kocevski et al. 2015). Kocevski et al. (2015) were among the first to attempt a careful investigation of such a relationship by selecting one of the largest samples of obscured AGNs of its time using multiple deep-field X-ray data sets. However, different from our work, they only used one HST NIR band (F160W) and employed a smaller number of human classifiers (two), and their statistical analysis did not consider the biases we work to address here. Additionally, the control sample in Kocevski et al. (2015) consisted of unobscured X-ray-selected AGNs. They were selected to match their obscured sample in both redshift and X-ray luminosity only. Conversely, in this work, our control sample consists of inactive galaxies. This is important because unobscured AGNs may have a significant unresolved pointlike component in their images, thus making morphological classification and estimation of the stellar properties of host galaxies with bright point sources extremely difficult. Interestingly, as noted by these authors, when they removed the sources with point-source morphologies, the significance of the merger excess in the heavily obscured AGN sample dropped from 3.8σ to 2.5σ.

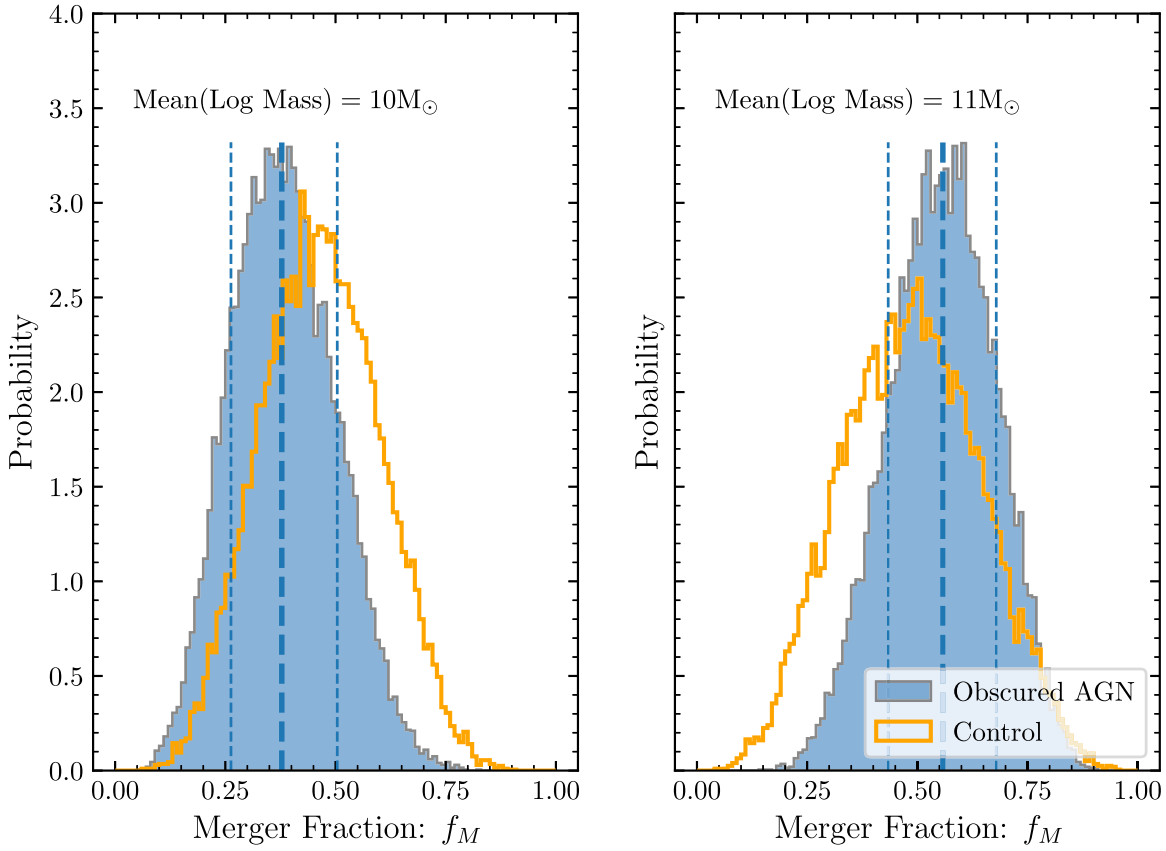

Figure 7. Merger probabilities of the non-SB obscured AGN and matched inactive galaxy control sample in two stellar mass bins. The blue filled histogram is the merger probability distribution of the obscured AGN sample, and the open orange histogram is the matched inactive galaxy sample. We split the non-SB obscured AGN sample on the median log stellar mass: $9.32 < \log(M_*\,[M_\odot]) < 10.7$ (20 objects) and $10.7 < \log(M_*[M_\odot]) < 11.32$ (20 objects). The left panel represents the merger probability distributions of the lower stellar mass bin ($\log(M_{*,\mathrm{mean}}) = 10\ M_\odot$), and the right panel shows the merger probability distributions for the higher stellar mass bin ($\log(M_{*,\mathrm{mean}}) = 11\ M_\odot$).

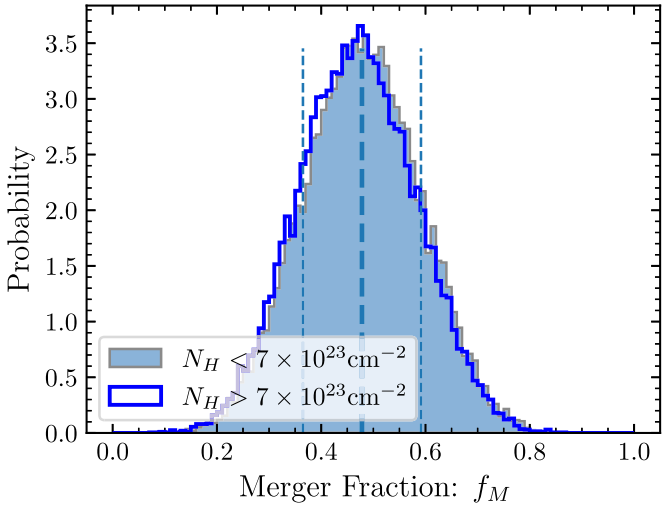

Figure 8. Merger probabilities of non-SB obscured AGNs in two N_{H} bins. The light blue filled histogram is for the non-SB obscured AGN sample with objects with $N_{\mathrm{H}} < 7 \times 10^{23}\,\mathrm{cm}^{-2}$, and the dark blue open histogram is for non-SB obscured AGNs with $N_{\mathrm{H}} > 7 \times 10^{23}\,\mathrm{cm}^{-2}$.

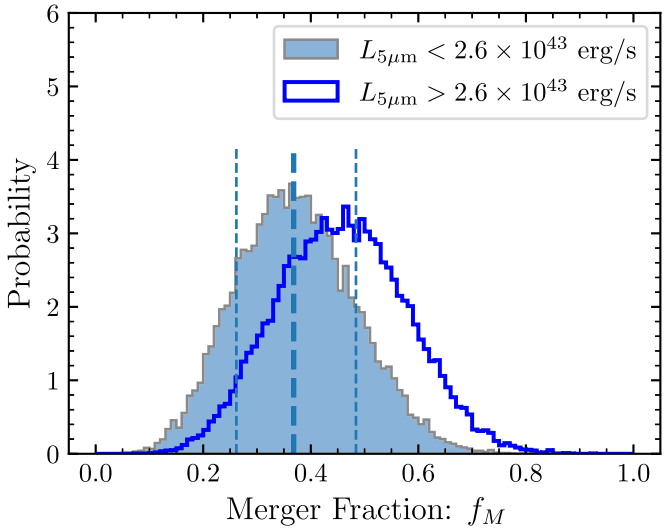

Figure 9. Merger probabilities of non-SB obscured AGNs in two L_{torus^*} bins. The light blue filled histogram is for the non-SB obscured AGN sample with objects with $L_{\mathrm{torus}^*} < 2.6 \times 10^{43}$ erg s^{-1}, and the dark blue open histogram is for non-SB obscured AGNs with $L_{\mathrm{torus}^*} > 2.6 \times 10^{43}$ erg s^{-1}

Another significant difference is that the SF properties were not determined prior to control sample creation. As mentioned in Section 2.1, both theoretically and observationally, there is a strong association between mergers and starbursting galaxies (Sanders & Mirabel 1996; Veilleux et al. 2009; Kartaltepe et al. 2012; Rodríguez Montero et al. 2019). Many AGN studies focusing on the morphology of AGN host galaxies do not properly remove SB galaxies from their samples. It is in fact very difficult to adequately take this into account, since large samples of AGNs with deep optical/UV imaging at the redshift distribution probed in this work usually lack the required high

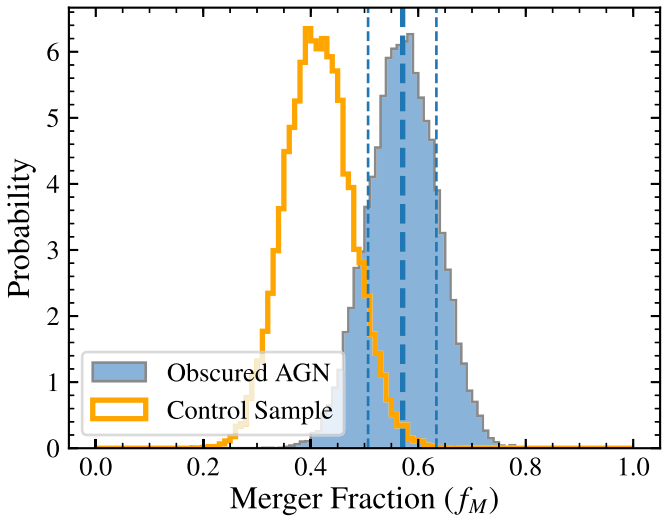

Figure 10. Including obscured AGNs with hosts undergoing an SB reveals the importance of including SF properties in the counterpart sample creation.

signal-to-noise ratio IR spectra to accurately detangle the SF and AGN contribution to the IR. If the AGN sample contains more (or fewer) starbursting galaxies than the control sample, a noncausal merger excess (or deficit) can be found in the obscured sample.

To check if the uneven inclusion of SB galaxies would generate any significant bias on our results, we rerun our analysis of non-SB obscured AGNs while including potential SB galaxies in the obscured sample. In Section 2.1.2, we identified 10 SBs in the HST-covered subsample of the L20 obscured AGN sample. We input these additional 10 obscured AGNs with SBs in their hosts into the non-SB obscured AGN sample used in this study while also including 10 (non-starbursting, non-SBs) redshift, and F160W matched to the control galaxy sample. We do to this to mimic the effect of studies that do not take into account the presences of SBs in their sample creation and may have an uneven number of SBs between their science and control samples. As seen in Figure 10, with the inclusion of only 10 starbursting galaxies, the obscured AGN merger fraction increases by 8%, and if the results were taken at face value, this would imply a 2σ excess in the merger fraction of the obscured AGN sample with respect to the control sample. However, this is only due to a bias resulting from the inclusion of the SB galaxies, not to any intrinsic physical association between obscured AGNs and mergers. In other words, we are only seeing the possible connection between SBs and mergers, and no information on the role of mergers in triggering AGNs could be derived by such an analysis. It remains to be seen whether the AGNs that are triggered by significant mergers are those with SBs in their host galaxies. Due to the lack of sufficient data at hand, we do not compare the merger fractions of obscured AGNs with SBs as compared to control galaxies with SBs.

Instead, as we have shown above, we find that heavily non-SB obscured AGNs (mean $N_{\rm H} = 1e24$ erg s^{-1}) are not associated in heavily merging systems more than their inactive galaxy counterparts. One major implication of our finding is that the cause of obscuration in most non-SB obscured AGNs does not seem to be linked to the funneling of large quantities of gas and dust due to a significant merger, as theorized by Hopkins et al. (2008) and others. The AGNs may also appear to be obscured due to the orientation of either the torus or the host galaxy itself. Star-forming, inactive galaxies are usually observed being characterized by column densities on the order of $>10^{23}$ cm^{-2} when viewed completely edge-on. A notable example of this is the Milky Way. At redshifts higher than this work (i.e., $z = 4$), where galaxies can be extremely dust-rich, Circosta et al. (2019) measured Compton-thick AGN-like obscuration (i.e., $N_{\rm H} > 10^{24}$ cm^{-2}) in AGN galaxies but determined the source of obscuration to be from the kpc scale ISM of the host galaxy itself.

In summary, our results disfavor the major merger–driven non-SB obscured AGN paradigm as the dominant process behind AGN triggering and the cause of the obscuration. As shown in L20, the population of obscured AGNs in this sample is representative of the low-to-moderate-luminosity regime of obscured AGNs. This regime makes up the predicted bulk of the obscured AGN population as estimated by X-ray background models (Gilli et al. 2007). The similar merger rates for the obscured sources and the control sample indicate that most obscured AGNs are not correlated with major mergers. Our work does not rule out whether the merger paradigm works for the highest end of the AGN luminosity or SMBH mass distribution, but other works do (i.e., Villforth et al. 2017; Marian et al. 2019). As previously mentioned, the region of the AGN luminosity parameter space our sample includes represents the bulk of AGN activity at these redshifts.

It is also possible that minor mergers play a role in triggering AGNs. Theoretically, these minor mergers and flybys may be able to trigger a disk instability that would ultimately cause the funneling of gas and dust toward the center (Hopkins & Hernquist 2006, 2009). At $z > 2$, simulations find that small mergers ($M1/M2 < 1/4$) are the most frequent (Rodriguez-Gomez et al. 2015). In contrast, McAlpine et al. (2020) found that galaxy mergers in the EAGLE simulations with mass ratios between 0.1 and 0.25 are not a statistically relevant fueling mechanism for SMBHs. These minor flybys and/or mergers are difficult to identify at these redshifts with the data in hand. Future work will entail exploring the fraction of minor mergers in obscured AGN systems and quantifying the ability of human classifiers to separate minor from major-merging systems. Additionally, we plan to carefully analyze the SF properties of AGNs within and without starbursting host galaxies in the context of a galaxy's morphology.

6. Summary and Conclusion

We test a key prediction of the AGN–merger paradigm that connects nuclear obscuration of AGNs as a consequence of a significant galactic merger. Using a sample of 40 nonstarbursting low-to-moderate-luminosity obscured AGNs in the GOODS-S field at $0.5 < z < 3.1$ derived from the deepest X-ray survey to date, we construct a study to test whether non-SB obscured AGNs are found predominantly in major-merging systems. We construct a redshift, magnitude-matched inactive galaxy control sample comprised of 40 nonstarbursting galaxies. Due to the higher redshifts probed in the sample, we are probing AGN host galaxies that are ill suited for the most common automated merger identification schemes; thus, we use a sample of 14 expert human classifiers to visually identify the merger status of each galaxy. We estimate each individual classifier's accuracy at identifying merging galaxies/postmerging systems and isolated galaxies. We calculate the probability of each galaxy being in either a merger or an isolated system where "merger" is defined as a galaxy that

can be in either a major merger, a minor merger, or a majorly disturbed system. We do not find any statistically significant evidence that non-SB obscured AGNs are predominantly found in systems with evidence of significant merging/postmerging features. We further split the sample into different bins of galaxy properties and confirm that it is not evidence for statistically significant merger enhancement in non-SB obscured AGN galaxies.

We thank the anonymous referee for the thoughtful insight and important contributions to this work. E.L.L. is supported by the STSCI's Director's Discretionary Fund with account No. D0101.90261. R.G. acknowledges support from the agreement ASI-INAF no. 2017-14-H.O. This research has made use of the NASA/IPAC Infrared Science Archive, which is operated by the Jet Propulsion Laboratory, California Institute of Technology, under contract with the National Aeronautics and Space Administration. This publication makes use of data products from the Wide-field Infrared Survey Explorer, which is a joint project of the University of California, Los Angeles, and the Jet Propulsion Laboratory/California Institute of Technology, funded by the National Aeronautics and Space Administration. This publication makes use of data products from the Two Micron All Sky Survey, which is a joint project of the University of Massachusetts and the Infrared Processing and Analysis Center/California Institute of Technology, funded by the National Aeronautics and Space Administration and the National Science Foundation. We acknowledge the extensive use of the following Python packages.

Software: pandas, scipy, ipython, matplotlib, pymc (Hunter 2007; Pérez & Granger 2007; McKinney 2010; Virtanen et al. 2020, respectively). This research made use of `astropy`, a community-developed core Python package for astronomy (Astropy Collaboration et al. 2013).

Appendix
Demo Survey

In Figure 11, we show the demo survey with answers given to the human classifiers prior to classifying the full sample.

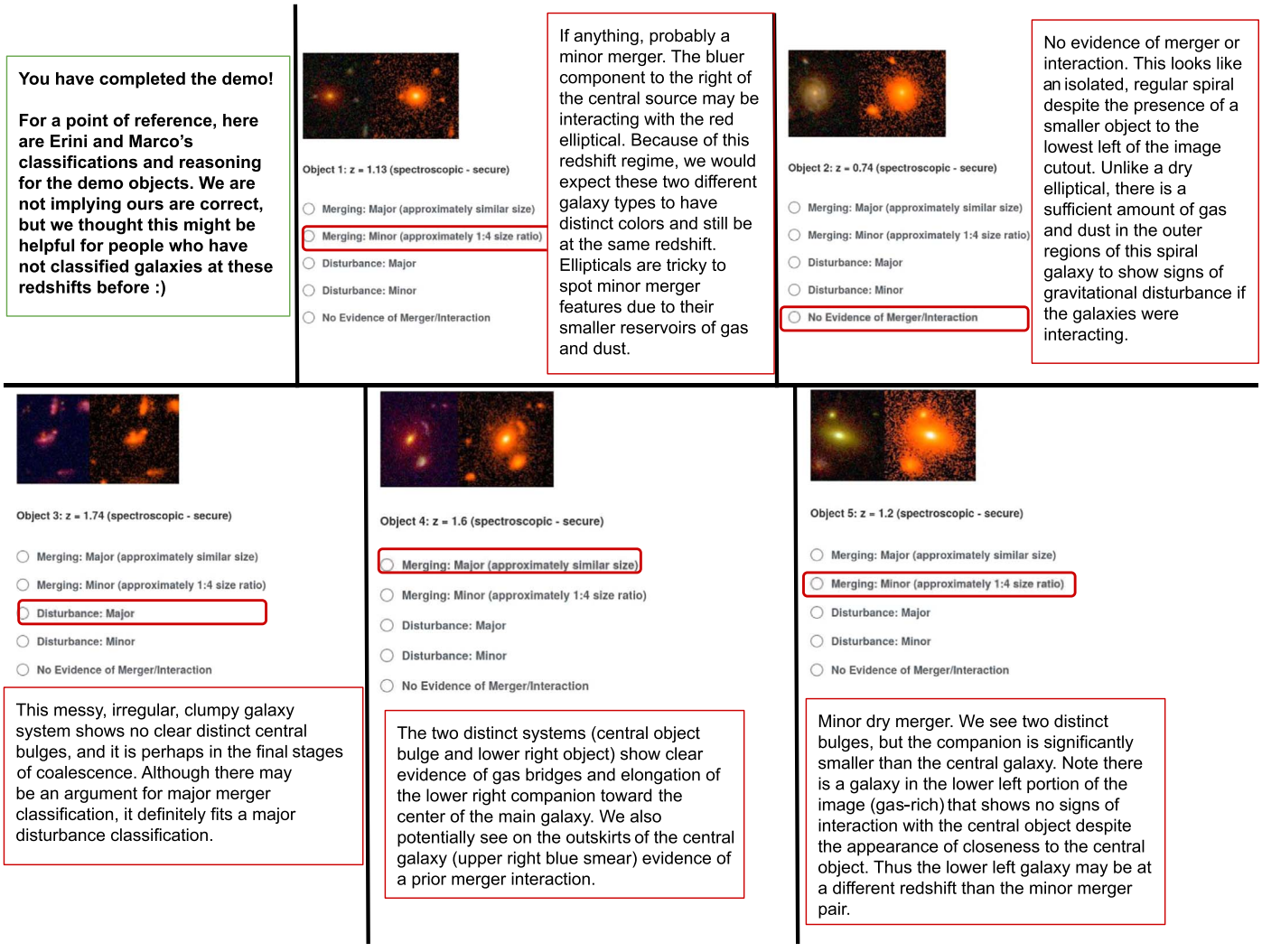

Figure 11. Demo survey. We provided a demo survey of five objects (not used in the MOOAGN sample) to all classifiers to provide a reference framework of the classification options and data quality. At the end of the demo survey, we give some example justifications of why one would classify an object, as noted by the red boxes.

ORCID iDs

Erini L. Lambrides https://orcid.org/0000-0003-3216-7190
Marco Chiaberge https://orcid.org/0000-0003-1564-3802
Timothy Heckman https://orcid.org/0000-0001-6670-6370
Allison Kirkpatrick https://orcid.org/0000-0002-1306-1545
Eileen T. Meyer https://orcid.org/0000-0002-7676-9962
Kirsten Hall https://orcid.org/0000-0002-4176-845X
Arianna Long https://orcid.org/0000-0002-7530-8857
Duncan J. Watts https://orcid.org/0000-0002-5437-6121
Roberto Gilli https://orcid.org/0000-0001-8121-6177
Raymond Simons https://orcid.org/0000-0002-6386-7299
Kirill Tchernyshyov https://orcid.org/0000-0003-0789-9939
Vicente Rodriguez-Gomez https://orcid.org/0000-0002-9495-0079
Fabio Vito https://orcid.org/0000-0003-0680-9305
Alexander de la Vega https://orcid.org/0000-0002-6219-5558
Colin Norman https://orcid.org/0000-0002-5222-5717

References

Aird, J., Coil, A. L., Georgakakis, A., et al. 2015, MNRAS, 451, 1892
Astropy Collaboration, Robitaille, T. P., Tollerud, E. J., et al. 2013, A&A, 558, A33
Bower, R. G., Benson, A. J., Malbon, R., et al. 2006, MNRAS, 370, 645
Brandt, W. N., & Hasinger, G. 2005, ARA&A, 43, 827
Brown, A., Nayyeri, H., Cooray, A., et al. 2019, ApJ, 871, 87
Brown, L. D., Cai, T. T., & DasGupta, A. 2001, StaSc, 16, 101
Calzetti, D., Wu, S. Y., Hong, S., et al. 2010, ApJ, 714, 1256
Cattaneo, A., Blaizot, J., Devriendt, J., & Guiderdoni, B. 2005, MNRAS, 364, 407
Ceverino, D., Klypin, A., Klimek, E. S., et al. 2014, MNRAS, 442, 1545
Chiaberge, M., Gilli, R., Lotz, J. M., & Norman, C. 2015, ApJ, 806, 147
Circosta, C., Vignali, C., Gilli, R., et al. 2019, A&A, 623, A172
Comastri, A., Ranalli, P., Iwasawa, K., et al. 2011, A&A, 526, L9
Cortijo-Ferrero, C., González Delgado, R. M., Pérez, E., et al. 2017, A&A, 607, A70
Croton, D. J., Springel, V., White, S. D. M., et al. 2006, MNRAS, 365, 11
Dai, Y. S., Wilkes, B. J., Bergeron, J., et al. 2018, MNRAS, 478, 4238
Davies, L. J. M., Robotham, A. S. G., Driver, S. P., et al. 2015, MNRAS, 452, 616
Donley, J. L., Kartaltepe, J., Kocevski, D., et al. 2018, ApJ, 853, 63
Donley, J. L., Koekemoer, A. M., Brusa, M., et al. 2012, ApJ, 748, 142
Elbaz, D., Dickinson, M., Hwang, H. S., et al. 2011, A&A, 533, A119
Ellison, S. L., Mendel, J. T., Scudder, J. M., Patton, D. R., & Palmer, M. J. D. 2013, MNRAS, 430, 3128
Ellison, S. L., Viswanathan, A., Patton, D. R., et al. 2019, MNRAS, 487, 2491
Fiore, F., Puccetti, S., Brusa, M., et al. 2009, ApJ, 693, 447
Gabor, J. M., Impey, C. D., Jahnke, K., et al. 2009, ApJ, 691, 705
Gandhi, P., Horst, H., Smette, A., et al. 2009, A&A, 502, 457
Gao, F., Wang, L., Pearson, W. J., et al. 2020, A&A, 637, A94
Georgakakis, A., Coil, A. L., Laird, E. S., et al. 2009, MNRAS, 397, 623
Gilli, R., Comastri, A., & Hasinger, G. 2007, A&A, 463, 79
Glikman, E., Simmons, B., Mailly, M., et al. 2015, ApJ, 806, 218
Grogin, N. A., Conselice, C. J., Chatzichristou, E., et al. 2005, ApJL, 627, L97
Grogin, N. A., Kocevski, D. D., Faber, S. M., et al. 2011, ApJS, 197, 35
Guo, Y., Ferguson, H. C., Giavalisco, M., et al. 2013, ApJS, 207, 24
Heckman, T. M., & Best, P. N. 2014, ARA&A, 52, 589
Hibbard, J. E., & van Gorkom, J. H. 1996, AJ, 111, 655
Hopkins, P. F., & Hernquist, L. 2006, ApJS, 166, 1
Hopkins, P. F., & Hernquist, L. 2009, ApJ, 694, 599
Hopkins, P. F., Hernquist, L., Cox, T. J., et al. 2006, ApJS, 163, 1
Hopkins, P. F., Hernquist, L., Cox, T. J., & Kereš, D. 2008, ApJS, 175, 356
Houck, J. R., Soifer, B. T., Weedman, D., et al. 2005, ApJL, 622, L105
Hunter, J. D. 2007, CSE, 9, 90
Jogee, S. 2006, in Physics of Active Galactic Nuclei at all Scales, ed. D. Alloin, Vol. 693 (Berlin: Springer), 143
Kartaltepe, J. S., Dickinson, M., Alexander, D. M., et al. 2012, ApJ, 757, 23
Kirkpatrick, A., Pope, A., Alexander, D. M., et al. 2012, ApJ, 759, 139
Kirkpatrick, A., Pope, A., Sajina, A., et al. 2015, ApJ, 814, 9
Kocevski, D. D., Brightman, M., Nandra, K., et al. 2015, ApJ, 814, 104
Koekemoer, A. M., Faber, S. M., Ferguson, H. C., et al. 2011, ApJS, 197, 36
Koss, M., Mushotzky, R., Veilleux, S., & Winter, L. 2010, ApJL, 716, L125
Kriek, M., van Dokkum, P. G., Labbé, I., et al. 2009, ApJ, 700, 221
Lacy, M., Nyland, K., Mao, M., et al. 2018, ApJ, 864, 8
Lambrides, E., Watts, D. J., Chiaberge, M., et al. 2021, ApJ, 919, 43
Lambrides, E. L., Chiaberge, M., Heckman, T., et al. 2020, ApJ, 897, 160
Lambrides, E. L., Petric, A. O., Tchernyshyov, K., Zakamska, N. L., & Watts, D. J. 2019, MNRAS, 487, 1823
Lansbury, G. B., Gandhi, P., Alexander, D. M., et al. 2015, ApJ, 809, 115
Laurent, O., Mirabel, I. F., Charmandaris, V., et al. 2000, A&A, 359, 887
Liu, T., Tozzi, P., Wang, J.-X., et al. 2017, ApJS, 232, 8
Lotz, J. M., Primack, J., & Madau, P. 2004, AJ, 128, 163
Luo, B., Brandt, W. N., Xue, Y. Q., et al. 2010, ApJS, 187, 560
Luo, B., Brandt, W. N., Xue, Y. Q., et al. 2017, ApJS, 228, 2
Marian, V., Jahnke, K., Mechtley, M., et al. 2019, ApJ, 882, 141
Mateos, S., Alonso-Herrero, A., Carrera, F. J., et al. 2013, MNRAS, 434, 941
McAlpine, S., Harrison, C. M., Rosario, D. J., et al. 2020, MNRAS, 494, 5713
McKinney, W. 2010, in Proc. of the 9th Python in Science Conf., ed. S. van der Walt & J. Millman (Austin, TX: SciPy), 56
Momcheva, I. G., Brammer, G. B., van Dokkum, P. G., et al. 2016, ApJS, 225, 27
Moreno, J., Torrey, P., Ellison, S. L., et al. 2019, MNRAS, 485, 1320
Nenkova, M., Sirocky, M. M., Nikutta, R., Ivezić, Ž, & Elitzur, M. 2008, ApJ, 685, 160
Pearson, W. J., Wang, L., Alpaslan, M., et al. 2019, A&A, 631, A51
Pérez, F., & Granger, B. E. 2007, CSE, 9, 21
Rodighiero, G., Daddi, E., Baronchelli, I., et al. 2011, ApJL, 739, L40
Rodríguez Montero, F., Davé, R., Wild, V., Anglés-Alcázar, D., & Narayanan, D. 2019, MNRAS, 490, 2139
Rodriguez-Gomez, V., Genel, S., Vogelsberger, M., et al. 2015, MNRAS, 449, 49
Rosario, D. J., McIntosh, D. H., van der Wel, A., et al. 2015, A&A, 573, A85
Sanders, D. B., & Mirabel, I. F. 1996, ARA&A, 34, 749
Schawinski, K., Treister, E., Urry, C. M., et al. 2011, ApJL, 727, L31
Scholz, F. W., & Stephens, M. A. 1987, J. Am. Stat. Assoc., 82, 918
Schreiber, C., Pannella, M., Elbaz, D., et al. 2015, A&A, 575, A74
Simons, R. C., Kassin, S. A., Snyder, G. F., et al. 2019, ApJ, 874, 59
Skelton, R. E., Whitaker, K. E., Momcheva, I. G., et al. 2014, ApJS, 214, 24
Snyder, G. F., Lotz, J., Moody, C., et al. 2015, MNRAS, 451, 4290
Stern, D. 2015, ApJ, 807, 129
Stern, D., Assef, R. J., Benford, D. J., et al. 2012, ApJ, 753, 30
Stern, D., Eisenhardt, P., Gorjian, V., et al. 2005, ApJ, 631, 163
Treister, E., Schawinski, K., Urry, C. M., & Simmons, B. D. 2012, ApJL, 758, L39
Urrutia, T., Lacy, M., & Becker, R. H. 2008, ApJ, 674, 80
Veilleux, S., Rupke, D. S. N., Kim, D. C., et al. 2009, ApJS, 182, 628
Villforth, C., Hamann, F., Rosario, D. J., et al. 2014, MNRAS, 439, 3342
Villforth, C., Hamilton, T., Pawlik, M. M., et al. 2017, MNRAS, 466, 812
Virtanen, P., Gommers, R., Oliphant, T. E., et al. 2020, Nat. Methods, 17, 261
Xue, Y. Q., Luo, B., Brandt, W. N., et al. 2011, ApJS, 195, 10